Effect of Gold Nanoparticle Aggregation on Cell Uptake and Toxicity

Alexandre Albanese[†] and Warren C.W. Chan[†,‡,§,*]

[†]Institute of Biomaterials and Biomedical Engineering, Terrence Donnelly Centre for Cellular and Biomolecular Research, Materials Science and Engineering, University of Toronto, 160 College Street, Toronto, Ontario, Canada M5S 3E1, [‡]Chemical Engineering and Applied Chemistry, University of Toronto, 200 College Street, Toronto Ontario, Canada M5S 3E5, and [§]Department of Chemistry, University of Toronto, 80 St. George Street, Toronto, Ontario, Canada M5S 3H6

ABSTRACT Aggregation appears to be a ubiquitous phenomenon among all nanoparticles and its influence in mediating cellular uptake and interactions remain unclear. Here we developed a simple technique to produce transferrin-coated gold nanoparticle aggregates of different sizes and characterized their uptake and toxicity in three different cell lines. While the aggregation did not elicit a unique toxic response, the uptake patterns were different between single and aggregated nanoparticles. There was a 25% decrease in uptake of aggregated nanoparticles with HeLa and A549 cells in comparison to single and monodisperse nanoparticles. However, there was a 2-fold increase in MDA-MB 435 cell uptake for the largest synthesized aggregates. These contrasting results suggest that cell type and the mechanism of interactions may play a significant role. This study highlights the need to investigate the behavior of aggregates with cells on a case-by-case basis and the importance of aggregation in mediating targeting and intracellular trafficking.

KEYWORDS: gold nanoparticles · transferrin · uptake · endocytosis · aggregation · cytotoxicity · TEM

There is currently a significant effort to elucidate the interactions of nanoparticles with molecules, cells, and tissues.[1] These studies could provide a foundation for engineering the next generation of nontoxic nanomaterials that can effectively target and accumulate in diseased cells. This would lead to improvements in diagnostic imaging or therapeutic responses using nanoparticles as carriers, contrast agents, or therapeutic agents. Researchers started to investigate the effect of a nanoparticle's size,[2−4] shape,[5,6] surface charge,[7,8] and chemical composition[9] on intracellular trafficking, toxicity, and gene expression. While researchers cannot generalize correlative relationships between the nanoparticle physicochemical properties with specific biological responses, nanomaterials on a case-by-case basis have been demonstrated to elicit interesting biological responses, kinetics, and transport. For example, a change in the size of spherical gold nanoparticles coated with the protein Herceptin can lead to changes in the protein's binding avidity to the receptor target, cellular uptake, gene expression, and cell death.[4] Surface charge of cerium oxide nanoparticles influenced cellular localization and toxicity profile.[10] The transport of noncationic quantum dots from the lung to the mediastinal lymph nodes and clearance *via* the kidney was dependent upon size.[11,12]

When working with nanoparticles, it is always crucial to quantify the morphology, size, uniformity, and dispersity postsynthesis before attempting experiments. However, they may aggregate in cell culture media due to exposure to ions and protein which may cause unexpected results.[6,13−16] Aggregation occurs when the van der Waals attractive forces between particles are greater than the electrostatic repulsive forces produced by the nanostructure surface.[17,18] First, high concentration of ions in biological media can decrease the screening length of charged chemical groups on the nanoparticle surface. Second, the high protein content will eventually cause a thermodynamically favored replacement of surface-associated molecules with serum proteins.[19] The destabilization of the nanoparticle surface by both these mechanisms will inevitably cause a population of well-characterized nanoparticles dispersed in a buffered solution to aggregate/agglomerate in a biological medium such as blood, saliva, lung surfactant, or cell culture media.

More recent studies have attempted to coat nanoparticles with a stabilizing shell consisting of PEG, proteins, DNA, *etc.* Although these stabilized nanoparticles do not aggregate in the short term, several experiments have demonstrated eventual aggregation both *in vitro*[14] and *in vivo*.[20] Electron microscopy imaging has revealed the majority of nanoparticle aggregates

* Address correspondence to warren.chan@utoronto.ca.

Received for review February 23, 2011 and accepted June 7, 2011.

Published online June 21, 2011
10.1021/nn2007496

to be heterogeneous in both size and shape.[1−3] The presence of unwanted aggregates in synthesized nanomaterials can presumably affect the experimental reproducibility in biological applications and impede the targeting efficiency of nanoparticles to cells and tissues. Furthermore, aggregation/agglomeration of nanomaterials can affect the degree of uptake and toxicity based on the nanoparticle composition and the cell type. All of these studies were designed to mimic environmental exposure to industrial byproducts such as cerium oxide,[21] carbon nanotubes,[22] metal oxides,[23] *etc*. This is the first study to examine the effect of protein-coated aggregates on cellular interactions. Several obstacles have prevented this type of study in the past. First, most of the previous work has been done with agglomerated nanomaterials produced from "the top down" where various states of nanoparticle dispersion are achieved by altering sonication, power and time. These agglomerates are not likely to mimic aggregates occurring *in vivo* but rather model aggregates formed prior to exposure into biological media. Second, none of the previous studies used an actively targeting nanoparticle. This is likely due to the inability to synthesize actively targeting nanoparticle aggregates of various sizes. Here we developed a simple strategy to create actively targeting gold nanoparticle aggregates and used them to systematically evaluate the effect of aggregate size on uptake kinetics and toxicity on three cell lines expressing varying levels of the target receptor.

RESULTS AND DISCUSSION

There are a number of controlled techniques to assemble nanoparticles into aggregates. These techniques include aliphatic α,ω-dithiols,[24,25] light-induced self-assembly,[26] DNA-directed assembly,[27−32] and DNA cross-linking[33] to induce assembly of nanoparticles to form well-organized assembled structures of defined geometric structures (hexagons,[26] cubes,[27,28] and spheres).[34] However, "naturally" occurring nanoparticle aggregates are not perfect structures and are not homogeneous, and the results of studying the interactions of these well-defined aggregate structures may not be representative of the interactions of aggregates with biological systems. We therefore developed a crude but simple method to prepare different sized nanoparticle aggregates by manipulating the kinetics and stoichiometry of salt, proteins, and gold nanoparticles (AuNPs). As a model protein, we used transferrin because the iron-transporting transferrin protein is typically taken up by cells through the process of receptor-mediated endocytosis, can be overexpressed in cancer cells and has been used as targeting molecule for contrast agents or drug molecules.[35−40]

The reactants of the aggregates were 16 nm AuNPs coated with citric acid,[41] NaCl, and transferrin. When NaCl is added to water, it dissociates into Na^+ and Cl^-,

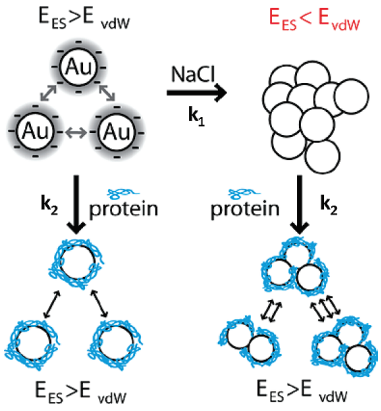

Figure 1. Scheme of aggregation mechanism. NaCl neutralizes the stabilizing electrostatic forces (E_{ES}) on the citrate-capped AuNPs, and this causes the van der Waals forces (E_{vdW}) to drive aggregate formation. When protein is added to this reaction, it can bind onto the surface of AuNPs and early aggregates and stabilizes them from NaCl, which prevents additional aggregation.

and Na^+ binds to the carboxylic acid on the citric acid groups at the AuNP surface, neutralizes the surface charge, and induces the instantaneous and irreversible aggregation of NPs into large structures that sediment out of solution as a dark gray precipitate (Figure 1). The use of NaCl in aggregate synthesis has already been demonstrated for both gold and other types of nanoparticles.[42,43] However, to control aggregate size and prevent precipitation of AuNPs, it was necessary to stabilize early aggregates and limit NP assembly to defined aggregate sizes. Preventing NaCl-induced aggregation is possible by adsorbing proteins onto the AuNP surface.[44] By simultaneous addition of NaCl and transferrin in various proportions, we were able to determine the conditions required to obtain nonprecipitating NP aggregates of various sizes. Using this system, it is possible to adjust the rates of both AuNP aggregation by NaCl (k_1) and AuNP stabilization by transferrin (k_2). When conditions are optimized where $k_1 > k_2$, the brief time between surface charge neutralization by Na^+ and adsorption of transferrin creates a moment of cluster−cluster diffusion-limited aggregation. In aqueous solution, diffusion (Brownian motion) is the predominant force driving NP movement and can be used to calculate aggregation kinetics using Smoluchowski's coagulation equation.[45,46] Diffusion-limited aggregation is a well-characterized process which produces predictable fractal structures.[42,47] At the end of this transient diffusion-limited aggregation, protein adsorption will stabilize AuNPs from further aggregation. To fully quench the aggregation reaction, we added additional transferrin after 1 min of reaction (see Methods section). It should be noted that although the words "agglomerate" and "aggregate" are often used interchangeably, we specifically chose to use aggregate since the NaCl-induced agglomeration of AuNPs is to our knowledge irreversible. Since

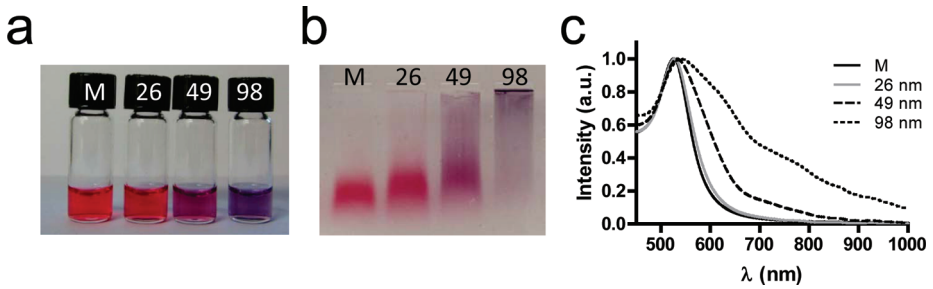

Figure 2. Characterization of aggregates. (a) Appearance of monodisperse (M; 0 mM NaCl), 26 nm (25 mM NaCl), 49 nm (100 mM NaCl), and 98 nm (400 mM NaCl) aggregates. (b) Gel shift assay of aggregates; electrophoresis was performed in 0.5% agarose migrated at 50 V for 2 h at 4 °C. (c) UV−vis spectra of aggregates that were prepared according to the protocol outlined in the Methods section and washed twice with 0.1% BSA.

TABLE 1. Characterization of Materials Used in the Experiments Presented[a]

		UV−vis	DLS		TEM				
		λmax (nm)	*d* (nm)	PDI	*d* (nm)	standard deviation	*N*	standard deviation	*n*
AuNPs	15 nm	517.5	17.7	0.052	16.22	1.09			148
	30 nm	525.0	31.28	0.116	31.55	3.72			262
	45 nm	528.0	45.05	0.049	44.54	5.39			95
TF-AuNP Aggregates	M[b]	525	28.80	0.109	21.38	5.08	0.96	0.33	764
	26 nm[b]	526.5	31.97	0.235	26.43	11.39	1.26	0.78	1729
	49 nm[b]	532.5	65.71	0.233	48.83	33.84	3.36	3.95	2753
	98 nm[b]	537.5	171.46	0.255	97.69	87.68	12.52	19.82	543

[a] Top of the table shows data from bare AuNPs postsynthesis. Bottom of the table shows data from transferrin-functionalized aggregates. [b] TEM size was determined using ImageJ macro described in the Methods section.

NaCl is the force behind aggregate assembly and our experiments reveal relatively long stability of synthesized aggregates (*vide infra*), we can confidently describe our nanomaterials as aggregates.

Aggregates were produced by fixing AuNP and transferrin concentrations at 2.6 nM (1.6×10^{12} AuNP/mL) and 64 nM (5 μg/mL), respectively, and varying the NaCl concentration between 0 and 400 mM. AuNP aggregation occurred as evidenced by an instantaneous color change from red to purple (Figure 2a). Electrophoresis confirmed the presence of aggregates using our synthesis method (outlined in the Methods section) since samples prepared with NaCl showed a slower electrophoretic mobility than monodisperse AuNPs (Figure 2b). Analysis of the UV−vis absorbance spectra revealed a red shift in the main surface plasmon resonance band from 525 nm in samples with protein alone to 527, 533, and 538 nm when NaCl concentration was 25, 100, and 400 mM, respectively (Figure 2c, Table 1). We also detected the appearance of a second red-shifted band at 700 nm as the concentration of NaCl increased. This second band is characteristic of the interparticle coupling effect[48,49] where metal NPs in close proximity possess a longitudinal plasmon resonance that absorbs light of higher wavelength.

Dynamic light scattering (DLS) was used to determine average aggregate hydrodynamic diameters (Table 1, Figure S2 in the Supporting Information). Since light scattering is exponentially proportional to NP size, we report our DLS data as a percentage of total volume and not percentage of measured intensity. Using this technique, we observe an ~11 nm increase in the hydrodynamic diameter of 16 nm AuNPs after addition of transferrin due to the presence of a protein corona. The radius of the AuNP plus protein corona would be 14.4 nm, which would include an 8.9 nm AuNP radius plus a 5.5 nm transferrin layer. Consistent with our other findings, DLS data revealed a NaCl-dependent increase in the average aggregate size, although large polydispersity indexes suggest a heterogeneous population. Due to the large polydispersity indexes (PDI in Table 1), we concluded DLS to be unreliable in determining the overall size distribution of the aggregates. DLS can also overestimate mean particle size due to the high scattering intensities of larger objects which makes our data difficult to interpret.[43] Another concern with the light scattering measurements is that our instrument uses a 633 nm laser, and the increased absorbance of this wavelength by aggregates makes it difficult to convert data as a percentage of intensity to percentage of volume. Also, accurate data regarding the precise scattering properties of AuNP aggregates in solution are not available.

Due to the uncertainty of the DLS data, we decided to establish a method based on TEM to improve the

accuracy in aggregate size measurements (Figure S3). Aggregate size was determined by analyzing multiple TEM images using ImageJ in order to determine the maximum diameter and surface area of each aggregate structure. To validate our method, the first step was to determine how many "false aggregates" were detected in monodisperse transferrin-coated 16 nm AuNP TEM images. Multiple experiments revealed that even at high concentrations transferrin-coated 16 nm AuNPs do not form aggregates after air drying on the TEM grid (Figure 3a). Once the TEM images were processed using our algorithm, we noticed ~5% of the monodisperse 16 nm AuNPs in close proximity to one another were detected as aggregates. The accuracy of our image analysis method was therefore estimated to be able to distinguish ~95% of the aggregates from single AuNPs. Since the majority of monodisperse AuNPs were not detected as aggregates using this method, we considered all aggregates observed by TEM as products of our synthesis method. This assumption that near-neighbors on the TEM image are covalently linked at relatively dilute conditions was previously used by Hussain *et al.*[50] and validated by our data.

Under TEM, the aggregates possessed a fractal-like morphology consistent with diffusion-limited aggregation.[42,45,46] The aggregates constituted a heterogeneous population of different sizes within a single preparation. Image analysis allowed us to estimate both the maximum diameter (Figure 3) and surface area for each aggregate. The maximum diameter was used since it is likely to represent more accurately the hydrodynamic diameter of each aggregate. The surface area was obtained in order to estimate the average number of AuNPs per aggregate (Figures S4 and S5). Due to the three-dimensional structure of aggregates, it is difficult to accurately determine the number of NPs per aggregate when they consist of more than 3–4 AuNPs. For this reason, we opted to measure the aggregates as a function of maximum diameter that can be accurately determined using TEM. Although the heterogeneity of the samples resulted in large standard deviations, there was a significant trend toward larger aggregates as the NaCl concentration increased ($p < 0.001$, ANOVA). This large polydispersity is characteristic of diffusion-limited aggregation and has been present in previous aggregate synthesis studies.[50,51] To work around the large polydispersity of our samples, we selected conditions that produced aggregates of different size ranges (Figure 3). For example, 25 mM NaCl produced some doublets and triplets among a predominantly monodisperse population; 100 mM NaCl produced samples where >80% of the sample is within the 20–80 nm size range; 400 mM NaCl generated aggregates where >60% aggregates are in the 80–200 nm size range. For simplification, the nomenclature we selected to represent the aggregates as a single number and not a size range in this article. This single number is aggregates' average size as determined by TEM (Table 1). For example, the aggregate size range of 20–80 nm is denoted as 49 nm.

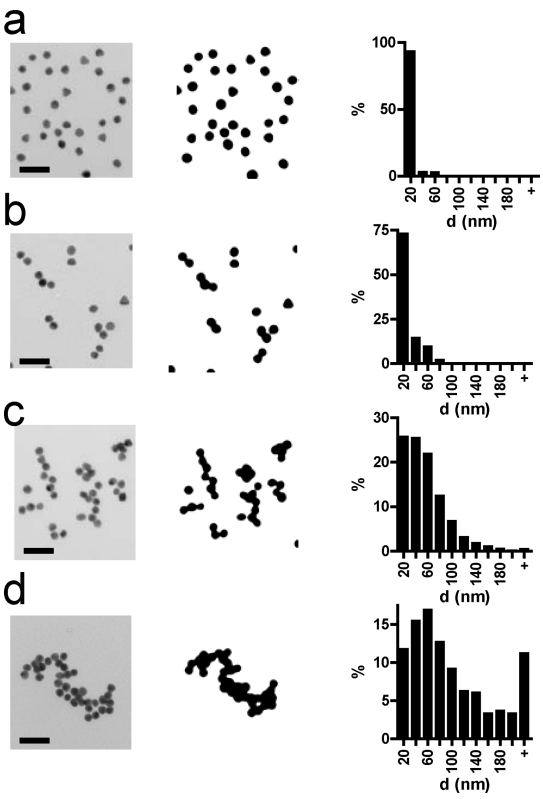

Figure 3. TEM-based sizing of aggregates. Appearance and size distribution of aggregates prepared with 0 (a), 25 (b), 100 (c), and 400 mM (d) NaCl. On the left, representative images were taken at 85 000× (scale bars represent 50 nm). In the middle, images were processed with the ImageJ macro used for aggregate sizing. On the right, histograms of maximum aggregate diameter were obtained using ImageJ. Data are presented as the percentage of all structures detected by TEM.

These different aggregate preparations presumably mimic the early and late stages of naturally occurring aggregation in biological environments where doublets and triplets appear initially followed by progressive growth of aggregates into larger structures. When NPs aggregate in a biological environment, local destabilization of the surface chemistry will cause multiple NPs to bind together. Therefore, destabilized regions will become the site of NP-to-NP interaction, whereas areas of intact surface chemistry will form the outer surface of the aggregates. In the case of actively targeting NPs, naturally occurring aggregates will possess a surface whose majority contains the active targeting moiety. To properly mimic naturally forming aggregates, we wanted to confirm the presence of transferrin on their surface. Sandwich enzyme-linked immunosorbent assays (ELISA) were used to confirm the presence of transferrin on the surface of aggregates (Figure S6). It should be noted that an equal amount of AuNPs were added to each well in the assay; however, it was impossible to quantify the number of AuNPs bound

to the capture antibody. Also, sandwich ELISA was designed to measure concentrations of soluble molecules, not proteins bound onto a surface. ELISA data should not be considered quantitative and were simply used in a qualitative context to confirm the presence of transferrin. Another concern that arose from producing aggregates was whether they continued to grow or broke apart over time. Once synthesized, aggregates were stable for at least 14 days in 0.1% BSA with no detectable change in UV−vis spectra or hydrodynamic diameter (Figures S7 and S8). We also confirmed that our aggregates were stable in cell culture media at 37 °C in 5% CO_2 for at least 8 h, which is the longest cell incubation time in our experiments (Figure S9).

Once we were able to confirm the presence of transferrin and aggregate stability, cell uptake experiments were conducted. After preparing and characterizing our nanomaterials, aggregates were incubated with cultured cells and gold uptake was quantified using the technique of inductively coupled plasma-atomic emission spectroscopy (ICP-AES). Prior to incubation with cells, monodisperse AuNPs and aggregates were quantified using ICP-AES in order to determine each material's concentration. When comparing the different sized aggregates and monodisperse nanoparticles, we chose to use a constant number of AuNPs in our cell culture experiments. We added 1 mL of 0.2 nM monodisperse AuNPs (1.2×10^{11} NP/mL) and the equivalent mass of gold under various states of aggregation. Using this method, cells exposed to 100 individual AuNPs would be compared to 50 2-NP aggregates or one aggregate made up of 100 NPs. This approach generates experimental conditions where aggregate size is reversely proportional to concentration of structures in solution. These conditions mimic an experiment where 100 individual AuNPs are injected into an animal and progressively assemble into a single large aggregate.

The monodisperse and aggregated AuNPs were coated with the transferrin protein, which typically enters cells *via* the process of receptor-mediated endocytosis. We chose three commonly used human cell lines and quantified their expression of transferrin receptor (CD71) using flow cytometry. Results revealed that CD71 expression was HeLa > A549 > MDA-MB-435 cells (Figure S10). The amount of fluorescently labeled transferrin bound to the cell surface also correlated with CD71 expression (Figure S11). When we assessed the effect of aggregate size on uptake in HeLa cells, which express the highest levels of CD71, the total amount of AuNPs taken up by cells was reduced for 49 and 98 nm aggregates. There was a 25% decrease in the uptake of both the 49 and 98 nm aggregates in comparison to monodisperse nanoparticles (Figure 4a). For both the single and aggregated AuNPs, we observed a time dependent increase in uptake from 2 to 8 h. The 25% reduction in uptake of 49 and 98 nm aggregates was apparent at the 2 h time point

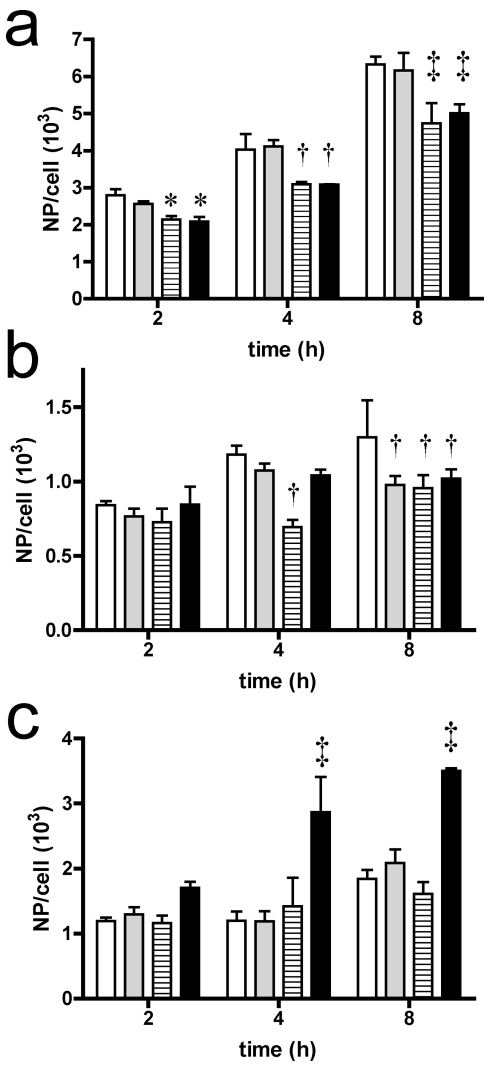

Figure 4. Aggregate uptake in HeLa, A549, and MDA-MB-435 cells. Uptake of monodisperse (white), 26 nm (gray), 49 nm (lines), and 98 nm (black) aggregates in HeLa (a), A549 (b) and MDA-MB-435 (c) cells. Cells were harvested at 2, 4, and 8 h and analyzed for gold content using ICP-AES. Aggregate uptake was compared to monodisperse AuNPs at each time point using ANOVA († $p < 0.01$, ‡ $p < 0.001$). Data represent the average of three replicate wells with standard deviation.

(Figure 4a; $p < 0.05$) and persisted until 8 h ($p < 0.001$). For A549 cells, all aggregates (26, 49, and 98 nm) show on average a 25% reduction in uptake compared to single AuNPs (Figure 4b). Behavior of A549 cells was comparable to HeLa cells with an additional reduction in the uptake of the smallest (26 nm) aggregates at 8 h. These findings suggest that A549 cells may be more selective in AuNP uptake. When comparing these two cell lines, the earliest detectable differences between the uptake of single and aggregated AuNPs occurred at 2 h for HeLa cells ($p < 0.05$) and at 4 h for A549 cells ($p < 0.01$) (Figure 4). It should be noted that, for A549 cells, detection of gold at 2 h (13−19 μg/L) and 4 h (17−30 μg/L) was slightly below our smallest standard (25 μg/L). Since we are

near the limit of detection of ICP-AES, uptake differences may not be detectable at early time points for A549 cells.[52] For these two cell lines, it can be concluded that transferrin-labeled aggregates will decrease AuNP uptake into cells.

The MDA-MB-435 cells displayed a different uptake trend in comparison to the HeLa and A549 cells. Surprisingly, the 98 nm aggregates show a 2-fold increase in uptake ($p < 0.001$) when compared to the smaller sized aggregates at 4 h. Interestingly, increased uptake is only apparent for the largest aggregates, suggesting that increased uptake only occurs above a certain size threshold not achieved by the 26 or 49 nm aggregate preparations. These findings were unexpected since theoretical models predict the optimal diameter for NP uptake to be ~50 nm in receptor-mediated endocytosis.[53−55] Since MDA-MB-435 cells possess the lowest expression of transferrin receptors, it is unlikely that large aggregates are using receptor-mediated endocytosis to enter the cells. In theory, large aggregates require more receptor−ligand interactions in order to drive the thermodynamic process of membrane wrapping around the aggregates.[53,54,56] Thus, increased uptake in MDA-MB-435 cells suggests that larger AuNP aggregates may enter cells through other mechanisms in addition to receptor-mediated endocytosis. To validate this hypothesis, we compared the uptake of monodisperse single and 98 nm aggregates in the presence or absence of 1 mg/mL transferrin. We hypothesized that, in the presence of a high transferrin concentration, the AuNPs would not enter the cells due to saturation of the CD71 receptors on the cell surface. High transferrin concentration was able to reduce uptake of monodisperse AuNPs by 91, 85, and 73% in HeLa, A549, and MDA-MB-435 cells, respectively (Figure 5). In contrast, free transferrin was much less efficient at blocking uptake of aggregates in all three cell lines. Whereas A549 and HeLa cells only show an appreciable reduction in uptake of 98 nm aggregates at 51 and 60%, respectively, MDA-MB 435 cells show a 10% reduction in uptake. These findings suggest that additional cell uptake pathways (in addition to transferrin receptor-mediated endocytosis) may be involved in the internalization of 98 nm aggregates. Although these additional pathways play a minor role in A549 and HeLa cells, it is apparent that MDA-MB-435 cells are highly efficient at receptor-independent uptake. It remains unclear, however, whether aggregates are entering MDA-MB-435 cells using a different cell surface receptor or are interacting nonspecifically with the cell membrane.

Next, we wanted to assess whether the observed uptake trends were unique to aggregates or simply a consequence of the aggregates' larger size compared to disperse AuNPs. We quantified uptake of monodisperse and single transferrin-coated AuNPs with diameters of 30, 45, and 100 nm in the three cell lines. All

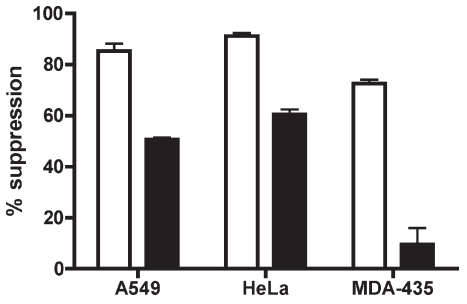

Figure 5. Inhibition of receptor-mediated uptake. Uptake of monodisperse AuNPs (white) and 98 nm aggregates (black) in the presence of 1 mg/mL transferrin. Data are presented as the "% suppression" when compared to controls where cells were incubated with monodisperse and 98 nm aggregates in the absence transferrin in solution.

samples were normalized to the same volume of gold in order to adequately mimic the inverse relationship between size and concentration in the aggregated samples. Cells were analyzed by ICP-AES, and data were calculated as the average mass of gold internalized per cell (pg/cell). Unfortunately, we were unable to adequately assess the internalization of 100 nm AuNPs since NPs of this size tend to quickly settle at the bottom of 6-well plates by 2−3 h. The rapid settling speed of large AuNPs can increase the local concentration of the AuNPs near the cell surface, and this may alter uptake kinetics.[57] In this comparative study, aggregated AuNPs did not follow the same trends as the size-matched spherical AuNPs. The uptake of different AuNP sizes followed the same trend for each cell line where the volume of internalized gold increases proportionally with AuNP diameter (Figure 6a). We conclude that aggregate uptake cannot be predicted by measuring the internalization of similar-sized monodisperse AuNPs. Other than the aggregates' increased diameter, various additional parameters can influence uptake. These include the high surface curvature of 16 nm AuNPs *versus* larger spherical particles, which lowers the density of targeting moieties on the gold surface.[4] Theoretical models suggest that ligand density may be crucial in cell uptake kinetics,[54,56] and since aggregates are made up of small 16 nm AuNP subunits, they likely possess a lower surface density of transferrin compared to size-matched spherical nanoparticles. Another factor to consider is that the irregular shapes of aggregates can possess aspect ratios larger than 1, and this is known to influence endocytosis rates.[6] Furthermore, the asymmetrical structure of aggregates can also increase the complexity of interactions with a cell's membrane. For example, a diamond-shaped aggregate made of four AuNPs can interact with a cell either at the tip of the aggregate where a single NP interacts with the cell membrane or at one of the edges where two AuNPs interact with the membrane (Figure 6b). Multivalent receptor-to-ligand interactions lead to an increase in binding avidity,[4] and in effect,

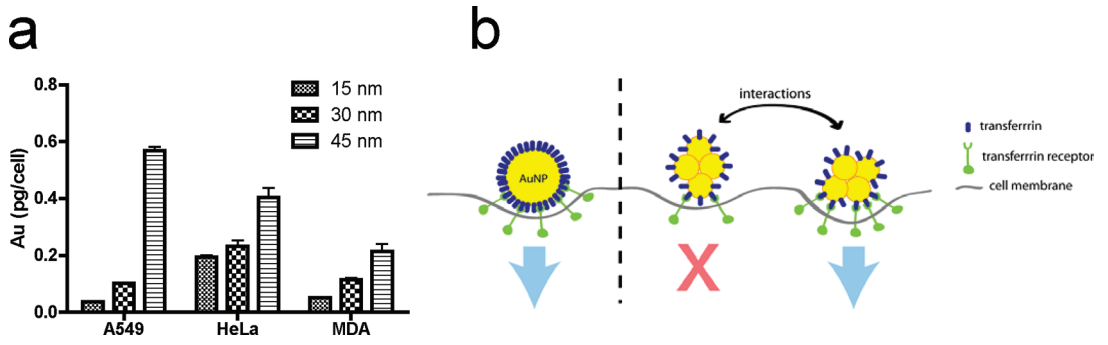

Figure 6. Uptake of spherical transferrin-coated AuNPs. (a) Amount of gold internalized per cell at 8 h. The A549, HeLa, and MDA-MB-435 cells were incubated with transferrin-coated spherical AuNPs whose size was similar to average aggregate sizes. All data represent the average of three replicate wells with standard deviation. (b) Scheme comparing uptake of 30 nm AuNP (left) with a diamond aggregate of similar size (right). Whereas the 30 nm AuNP has one way of interacting with the cell membrane, the aggregate has two possible interactions: tip or edge of the aggregate. When the aggregate's tip interacts with cell membrane, there is not enough free energy produced by ligand−receptor binding to drive uptake.

this affects the amount and rate of nanoparticle internalization, cellular signaling, and the availability of receptors during the endocytic process. The aggregates are non-uniform and could interact with cellular receptors through a variety of different multivalent interactions. In our example, a perfectly symmetrical diamond-shaped aggregate can interact in two different conformations with cell receptors. However, if there are asymmetrical aggregate conformations, the number of unique potential interactions with cell surface receptors will increase. This phenomenon makes it difficult to model uptake of aggregates and highlights the inability to predict a cell's response to aggregates by simply assuming a larger NP diameter.

On a broad scale, we observed two distinct responses to aggregated AuNPs: a small reduction or large increase in cellular uptake. For both HeLa and A549 cells, aggregate uptake occurs predominantly *via* receptor-mediated endocytosis and is less efficient compared to monodisperse AuNPs. The MDA-MB-435 cells have a highly efficient receptor-independent uptake mechanism for aggregates. To better understand the role of transferrin receptor in aggregate uptake, we compared uptake of monodisperse AuNPs and 98 nm aggregates at a series of concentrations in order to saturate receptor binding. For these experiments, we simplified our conditions by comparing MDA-MB-435 and HeLa cells since they possess distinct aggregate uptake mechanisms. The dose response experiments revealed that MDA-MB-435 cells maintained an increased uptake of 98 nm aggregates compared to monodisperse AuNPs at all concentrations tested (0.2−1.0 nM). We also determined the percentage of AuNPs taken up by the cells relative to the administered dose using the following equation:

$$\%\ \text{dose} = \frac{\text{total internalized NPs}}{\text{total NPs per well}}$$

For MDA-MB-435 cells, the data series for both disperse and aggregated NPs did not have a slope

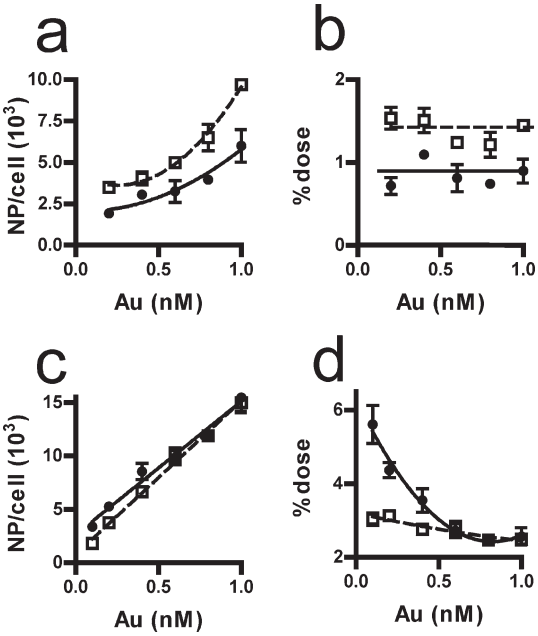

Figure 7. Aggregate dose response. Uptake of monodisperse AuNPs (closed circles) and 98 nm aggregates (open squares) at various concentrations in MDA-MB-435 cells (a,b) and HeLa cells (c,d). Data are plotted either as number of NP per cell (a,c) or percentage of total dose (b,d). Data represent the average of three replicate wells with standard deviation.

significantly different than zero. The percentage uptake of monodisperse AuNPs and 98 nm aggregates was constant at 0.84 and 1.39%, respectively (Figure 7b). HeLa cells, in contrast, did not maintain a reduced uptake of aggregates at all concentrations. Interestingly, above 0.6 nM, we could not detect any statistically significant difference in the uptake of monodisperse and aggregated AuNPs (Figure 7c). At concentrations below 0.6 nM, the difference in uptake between monodisperse and aggregated NPs is inversely proportional to AuNP concentration (Figure 7c). When uptake as a percentage of total administered dose was compared, HeLa cells consistently internalized ~2.5% of 98 nm

aggregates, independent of the concentration. In contrast, monodisperse AuNPs were internalized at 5.61% at 0.1 nM, and this decreased to 4.36, 3.54, and 2.62% for 0.2, 0.4, and 0.6 nM, respectively (Figure 7d). These findings suggest that high level of transferrin receptor expression on HeLa cells increases their affinity for monodisperse AuNPs at concentrations below 0.6 nM, and this caused higher uptake relative to aggregates. Once the effect of high receptor expression is saturated at 0.6 nM, aggregates and AuNPs behave similarly. These findings reveal two separate trends in the dose response to aggregates which is consistent with distinct uptake mechanisms.

To better understand how MDA-MB-435 and HeLa cells differ in their NP uptake mechanism, we analyzed TEM images of cells incubated with single AuNPs and 98 nm aggregates (Figure 8 and Figure S12 in the Supporting Information). These images confirm the internalization of both single and aggregated NPs in the two cell lines. All images taken of cells treated with either monodisperse or aggregated AuNPs clearly show that intracellular AuNPs are contained within vesicles. We were unable to find any AuNPs directly in the cytosol, and this suggests that trafficking inside the cells occurs predominantly through the endocytic pathway. In agreement with previous studies,[2,3] the majority of monodisperse AuNPs appeared as aggregates inside the vesicles of both HeLa and MDA-MB-435 cells. When we quantified the number of NPs per aggregate inside the vesicles, a mean aggregate size of 5.52 and 4.99 AuNPs per vesicle was observed for HeLa and MDA-MB-435 cells, respectively. The difference between the two cell lines was not found to be significant and reveals a similar sequestration of monodisperse AuNPs. When we analyzed the internalization of the 98 nm aggregates, MDA-MB-435 cells contained noticeably larger AuNP aggregates inside intracellular vesicles. HeLa cells had on average 14 AuNPs per aggregate, whereas MDA-MB-435 cells had 40 NPs per aggregate. Some previous studies have demonstrated that aggregated silica[58] and metal[59] nanoparticles remained on the cell surface membrane during uptake experiments. Our data reveal that aggregates are in fact internalized and do not simply remain associated with the cell surface.

Characterization of our nanomaterials before the cell experiments reveal that 98 nm aggregates possess an average of ~12.5 AuNPs per aggregate (N column in Table 1), and this value is comparable to the average size of internalized aggregates in HeLa cells. In contrast, the average size of internalized aggregates in MDA-MB-435 cells is approximately triple this value. In-depth analysis of our 98 nm aggregates reveals that aggregates larger than 40 AuNPs represent less than 10% of the entire population. Thus, the high frequency of large aggregates inside the MDA-MB-435 cells is due

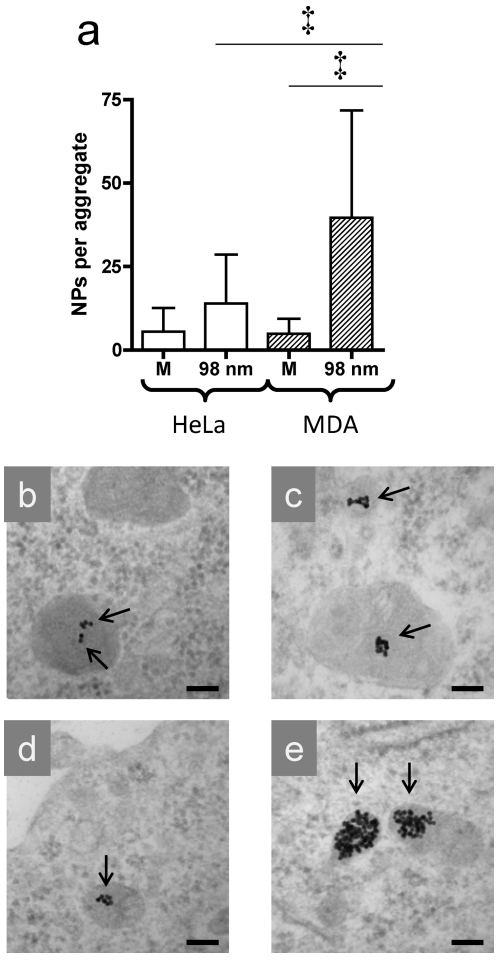

Figure 8. Size of internalized aggregates. (a) Average size of internalized NP aggregates inside vesicles of MDA-MB-435 and HeLa cells treated with monodisperse AuNPs or 98 nm aggregates. Data represent mean and SD of $n > 25$; ‡ denotes $p < 0.001$ using the statistical test ANOVA. Shown below are representative TEM images of HeLa cells incubated with monodisperse AuNPs (b) or aggregates (c) and MDA-MB-435 cells treated with monodisperse (d) or aggregated NPs (e). Bars represent 100 nm, and arrows highlight internalized AuNP aggregates.

to one of two possibilities. The first is that the largest aggregates in the extracellular environment are preferentially internalized; the second is that due to trafficking of aggregates in the endocytic pathway, an accumulation of large AuNP structures occurs inside the cells. Preferential internalization of the largest aggregates may be caused by their faster sedimentation rate compared to smaller nanostructures in solution. Sedimentation-driven uptake was previously reported in lung fibroblasts exposed to aggregated cerium oxide nanoparticles.[21] When we calculated the theoretical settling time of aggregates, our largest detected aggregate using TEM consisted of ~130 NPs and possessed a settling time of ~18 h in our reaction volume compared to ~160 h for a 16 nm AuNPs (calculations are outlined in the Supporting Information). Since 40 AuNP aggregates require a maximum of ~30 h to settle, our calculation suggests

that settling velocity of larger aggregates may increase uptake in MDA-MB-435 cells and lead to accumulation of large intracellular aggregates. Nevertheless, additional research will be required to elucidate the precise mechanism (*i.e.*, phagocytosis, pinocytosis, clathrin- or caveloe-dependent or independent endocytosis) of aggregate uptake in MDA-MB-435 cells. Some previous work with citrate-coated AuNPs suggests that uptake can occur *via* macropinocytosis, and this may be the predominant pathway of aggregate uptake in the MDA-MB-435 cells.[60]

On the basis of our findings, the effect of aggregation on cell uptake will be difficult to predict and will require a case-by-case analysis. Factors such as increased sedimentation rate, reduced diffusion speed, irregular morphology, and reduced concentration of aggregates will play a role in the uptake mechanism. Basic uptake experiments of disperse nanoparticles already demonstrate that no universal mechanism can describe the endocytosis of all nanomaterials. Instead, uptake depends on the physicochemical properties of the NP itself, the biological properties of the active-targeting ligand and the phenotype of the cell interacting with the NPs.[61] Elucidating the uptake mechanism of aggregates adds yet another level of complexity. At present, the limited data available for cellular uptake of nontargeting aggregates already eliminate the possibility of a "universal mechanism". One study reported no change in the lung's inflammatory response to aggregated or monodisperse AuNPs.[62] Another study describes no change in cytoplasmic uptake of tungsten carbide nanoparticles when agglomeration occurs.[63] Stark's group reports an increased uptake of agglomerated cerium oxide NPs in lung fibroblasts due to increased sedimentation.[21] In contrast, two separate studies show that aggregates localize to the cell membrane and are not internalized as efficiently as monodisperse AuNPs.[58,59] It is difficult to compare the aforementioned studies since each utilize different cells, nanomaterials, and experimental conditions. This highlights the need for more cohesion when designing future aggregate uptake studies, which will be required for a better understanding of nano–bio interactions.

After assessing the effect of aggregate size on cellular uptake, we also wanted to determine whether a change in the plasmonic properties of the AuNPs led to cellular toxicity. It has been speculated that the unique properties of NPs could cause various toxic responses.[64,65] We incubated the three cell lines at multiple aggregate concentrations for 72 h and assessed viability using the XTT assay. Our results show that cell viability is not affected by the presence of either monodisperse or aggregated AuNPs. Thus, the shift in the absorbance profile of the aggregated AuNPs did not influence toxicity to the cells (Figure 9 and Figure S13).

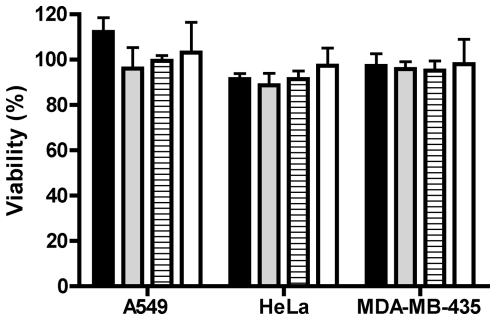

Figure 9. Toxicity of aggregates. Effect of aggregates on cell viability after 72 h incubation with monodisperse (black), 26 nm (gray), 49 nm (lines), and 98 nm (white) aggregates in three cell lines. Cell viability was determined at 72 h, by replacing cell media containing AuNPs with fresh media containing XTT and incubated for 2 h. All conditions were performed in triplicate. Data represent the average of three replicate wells with standard deviation.

CONCLUSIONS

This work is one of the first studies to examine the effect of aggregation on the cellular uptake of nanoparticles designed for a biomedical application. Previous studies on the interactions of aggregates with biological systems predominantly modeled their studies on the effect of unwanted exposure to nanoparticles from the environment. This is the first study to produce different aggregate samples which mimic the inevitable and progressive aggregation of active-targeting nanoparticles in biological media. Our findings demonstrate that multiple cellular responses are possible when nanomaterials are aggregated. Predicting a cell's response to a population of heterogeneous and asymmetrical aggregates is difficult since it depends on a number of parameters including expression of target receptor, endocytosis mechanism, and cell phenotype. Our work highlights the need to study the effect of aggregation for each NP designed and its target cell(s) in order to confidently predict the effects and safety of NP-based therapeutics. This subject is extremely important since aggregation appears to be an inevitable occurrence *in vivo* when designing long-circulating NPs. In the context of our current study, we can conclude that aggregation of transferrin-coated AuNPs reduces uptake *via* receptor-mediated endocytosis in HeLa and A549 cells. For MDA-MB-435 cells, aggregates enter the cells independently of transferrin receptor *via* unknown mechanisms, and this leads to the accumulation of large structures inside the cell's vesicles. This study not only highlights the need for more thorough studies regarding the downstream effects and toxicity of long-circulating nanomaterials that are prone to aggregation but also provides a synthesis technique for preparing nanoparticles aggregates (Figure S14). Continued

research in this topic will provide a better understanding of aggregation and will undoubtedly help the design of safe and effective nanoparticle platforms for biomedical applications.

METHODS

Instrumentation and Measurements. For absorbance spectra, a Shimadzu UV-1601 UV−vis spectrophotometer was used. For ELISA experiment measurements, we used a TECAN Sunrise plate reader. Transmission electron microscopy (TEM) images were obtained by deposition of a dilute particle solution onto carbon-coated copper grids and imaged using Hitachi HD2000 STEM at 200 kV(Hitachi Corp). Hydrodynamic diameter of different samples was measured by dynamic light scattering (DLS) on a 633 nm laser Nano ZS Zetasizer (Malvern), and all measurements are presented as a percentage of volume.

Gold Nanoparticles. Citrate-capped 16 nm gold NPs were synthesized using the Frens method[41] and sized using TEM. The 30, 45, and 100 nm single AuNPs were synthesized using hydroquinone-mediated growth of the 16 nm seeds.[66] The 30, 45, and 100 nm AuNPs were washed using a solution of 0.05% Tween-20 and 5 mM sodium citrate. Protein adsorption was performed using 5 mM citrate and 0.5, 1, and 4 mg/mL transferrin for 30, 45, and 100 nm NPs, respectively. The different transferrin concentrations used for each AuNP size were determined experimentally as the minimum amount of transferrin required for full surface coverage. Full surface coverage was assessed by stability of transferrin-coated AuNPs in 5% NaCl.[44] After 30 min incubation at 37 °C, bovine serum albumin (BSA) was added to the transferrin-coated AuNPs at a 0.1% concentration to ensure AuNP stability during centrifugation steps.[4] The AuNPs were washed twice following transferrin adsorption in a 0.1% BSA solution.

Aggregate Synthesis. For aggregate preparation, a 10× solution of NaCl and transferrin is added to 16 nm AuNPs directly after synthesis under vigorous vortex mixing. After 1 min, more Tf was added to achieve a final concentration of 50 μg/mL. After 10 min at room temperature, 0.1% BSA was added and incubated for an additional 10 min. Depending on the aggregate conditions, different centrifuge speeds were used. For 0 mM, samples were centrifuged at 15 000*g* for 15 min. For 25 mM, samples were centrifuged 6500*g* for 10 min. For 100 mM, samples were centrifuged at 500*g* for 10 min, and the supernatant was removed and centrifuged at 4500*g* for 10 min. For 400 mM, samples were centrifuged at 2500*g* for 10 min. The aggregate pellets were then resuspended in 0.1% BSA, sonicated in a water bath for 1 min, and centrifuged under the same conditions to further improve size distribution. After this step, aggregates were characterized and used in cell uptake experiments. For cell experiments, aggregates were quantified using ICP-AES. Using the total concentration of gold in solution, it was possible to calculate the concentration of monodisperse AuNPs using the mass of a 16 nm gold sphere.

TEM Image analysis. For TEM, 10 μL aliquots of aggregation preparations were placed on Formvar type B grids (Ted Pella), left for 15 min, and then wicked off. For each sample, 10−30 images were taken at 55 000×. The images were analyzed using ImageJ software using the following macro: Gaussian blur = 8, make binary, crop image, analyze particles (Figure S2). Data shown represent the maximum diameter (Ferret's diameter) for each cluster of NPs. The number of NPs per aggregate was determined by dividing the surface area of each aggregate by the theoretical 2D surface area of a 16 nm NP (πr^2). Although the aggregates are 3D structures, we believe this method is accurate for the measurement of small aggregates (2−6 NPs) when each AuNP is visible. For larger aggregates, their large three-dimensional structure makes it difficult to accurately determine the correct number of AuNPs per cluster. However, this method does provide a good estimate to the average composition of aggregates. For TEM images of cell vesicles, cell sections were prepared by fixing cell pellets in 2% glutaraldehyde in 0.1 M sodium cacodylate buffer, postfixed in 1% osmium tetroxide, dehydrated in a graded ethanol series followed by propylene oxide, and embedded in Quetol-Spurr resin. Sections that were 100 nm thick were cut on an RMC MT6000 ultramicrotome and stained with uranyl acetate and lead citrate. For each sample, three separate tissue sections (taken at a different depth) were placed on a TEM grid and imaged. Cells were incubated with 1 nM AuNPs for 8 h.

Cell Uptake and Toxicity. For NP uptake studies, HeLa and MDA-MB-435 cells were seeded 2×10^6 cells/well in 6-well plates and incubated overnight to allow for cell attachment. The A549 cells were seeded at 1×10^6 cells/well under the same conditions. After the overnight incubation, cell medium was removed and replaced with 1 mL of RPMI (A549, MDA-MB-435) or 1 mL of DMEM (HeLa) supplemented with 0.2% BSA. Cells were serum starved for 30 min, and fresh medium containing the AuNPs and 0.2% BSA was added. Experiments were performed in the absence of serum due to the large amounts of transferrin present in fetal bovine serum. Cells were incubated for 2, 4, or 8 h in the presence of AuNPs. At each time point, cell supernatant was removed and cells were washed three times with PBS. Samples were digested in 500 μL of nitric acid for 30 min at 70 °C, and diluted in 3 mL of ddH_2O. Gold uptake was quantified using ICP-AES. All conditions were performed in triplicate. The concurrent cell viability assay was performed using the XTT assay (Roche) in 96-well plates according to the manufacturer's instructions.

Acknowledgment. This work was supported by the Natural Sciences and Engineering Research Council of Canada (BiopSys Network, Grant No. NETGP35015-07; Discovery Grant, Grant No. RGPIN 288231-09), Canadian Insitute of Health Research (MOP-93532), the Canadian Foundation for Innovation and the Ministry of Research and Innovation in Ontario. A.A. was supported by the Ontario Graduate Scholarship. The authors would like to acknowledge D. Holmyard at the Mount Sinai Advanced Bioimaging Centre for TEM sample preparation of cell pellets.

Supporting Information Available: Additional figures and experimental procedures. This material is available free of charge *via* the Internet at http://pubs.acs.org.

REFERENCES AND NOTES

1. Nel, A. E.; Madler, L.; Velegol, D.; Xia, T.; Hoek, E. M. V.; Somasundaran, P.; Klaessig, F.; Castranova, V.; Thompson, M. Understanding Biophysicochemical Interactions at the Nano−Bio Interface. *Nat. Mater.* **2009**, *8*, 543–557.
2. Chithrani, B. D.; Chan, W. C. W. Elucidating the Mechanism of Cellular Uptake and Removal of Protein-Coated Gold Nanoparticles of Different Sizes and Shapes. *Nano Lett.* **2007**, *7*, 1542–1550.
3. Chithrani, B. D.; Ghazani, A. A.; Chan, W. C. W. Determining the Size and Shape Dependence of Gold Nanoparticle Uptake into Mammalian Cells. *Nano Lett.* **2006**, *6*, 662–668.
4. Jiang, W.; Kim, B. Y.; Rutka, J. T.; Chan, W. C. W. Nanoparticle-Mediated Cellular Response Is Size-Dependent. *Nat. Nanotechnol.* **2008**, *3*, 145–150.
5. Gratton, S. E.; Ropp, P. A.; Pohlhaus, P. D.; Luft, J. C.; Madden, V. J.; Napier, M. E.; DeSimone, J. M. The Effect of Particle Design on Cellular Internalization Pathways. *Proc. Natl. Acad. Sci. U.S.A.* **2008**, *105*, 11613–11618.
6. Qiu, Y.; Liu, Y.; Wang, L. M.; Xu, L. G.; Bai, R.; Ji, Y. L.; Wu, X. C.; Zhao, Y. L.; Li, Y. F.; Chen, C. Y. Surface Chemistry and Aspect Ratio Mediated Cellular Uptake of Au Nanorods. *Biomaterials* **2010**, *31*, 7606–7619.
7. Hauck, T. S.; Ghazani, A. A.; Chan, W. C. W. Assessing the Effect of Surface Chemistry on Gold Nanorod Uptake, Toxicity, and Gene Expression in Mammalian Cells. *Small* **2008**, *4*, 153–159.

8. Cho, E. C.; Xie, J.; Wurm, P. A.; Xia, Y. Understanding the Role of Surface Charges in Cellular Adsorption *versus* Internalization by Selectively Removing Gold Nanoparticles on the Cell Surface with a I2/Ki Etchant. *Nano Lett.* **2009**, *9*, 1080–1084.
9. Hussain, S. M.; Hess, K. L.; Gearhart, J. M.; Geiss, K. T.; Schlager, J. J. *In Vitro* Toxicity of Nanoparticles in Brl 3a Rat Liver Cells. *Toxicol. in Vitro* **2005**, *19*, 975–983.
10. Asati, A.; Santra, S.; Kaittanis, C.; Perez, J. M. Surface-Charge-Dependent Cell Localization and Cytotoxicity of Cerium Oxide Nanoparticles. *ACS Nano* **2010**, *4*, 5321–5331.
11. Choi, H. S.; Ashitate, Y.; Lee, J. H.; Kim, S. H.; Matsui, A.; Insin, N.; Bawendi, M. G.; Semmler-Behnke, M.; Frangioni, J. V.; Tsuda, A. Rapid Translocation of Nanoparticles from the Lung Airspaces to the Body. *Nat. Biotechnol.* **2010**, *28*, 1300–1303.
12. Choi, H. S.; Liu, W.; Misra, P.; Tanaka, E.; Zimmer, J. P.; Itty Ipe, B.; Bawendi, M. G.; Frangioni, J. V. Renal Clearance of Quantum Dots. *Nat. Biotechnol.* **2007**, *25*, 1165–1170.
13. Lacerda, S. H.; Park, J. J.; Meuse, C.; Pristinski, D.; Becker, M. L.; Karim, A.; Douglas, J. F. Interaction of Gold Nanoparticles with Common Human Blood Proteins. *ACS Nano* **2010**, *4*, 365–379.
14. Rausch, K.; Reuter, A.; Fischer, K.; Schmidt, M. Evaluation of Nanoparticle Aggregation in Human Blood Serum. *Biomacromolecules* **2010**, *11*, 2836–2839.
15. Maiorano, G.; Sabella, S.; Sorce, B.; Brunetti, V.; Malvindi, M. A.; Cingolani, R.; Pompa, P. P. Effects of Cell Culture Media on the Dynamic Formation of Protein–Nanoparticle Complexes and Influence on the Cellular Response. *ACS Nano* **2010**, *4*, 7481–7491.
16. Kim, D.; El-Shall, H.; Dennis, D.; Morey, T. Interaction of Plga Nanoparticles with Human Blood Constituents. *Colloids Surf. B* **2005**, *40*, 83–91.
17. Verwey, E. O. J. *Theory of the Stability of Lyophobic Colloids: The Interaction of Sol Particles Having an Electric Double Layer*; Elsevier: Amsterdam, 1948.
18. Derjaguin, B.; Landau, L. Theory of the Stability of Strongly Charged Lyophobic Sols and of the Adhesion of Strongly Charged Particles in Solutions of Electrolytes. *Prog. Surf. Sci.* **1993**, *43*, 30–59.
19. Lundqvist, M.; Stigler, J.; Elia, G.; Lynch, I.; Cedervall, T.; Dawson, K. A. Nanoparticle Size and Surface Properties Determine the Protein Corona with Possible Implications for Biological Impacts. *Proc. Natl. Acad. Sci. U.S.A.* **2008**, *105*, 14265–14270.
20. van Landeghem, F. K. H.; Maier-Hauff, K.; Jordan, A.; Hoffmann, K. T.; Gneveckow, U.; Scholz, R.; Thiesen, B.; Bruck, W.; von Deimling, A. Post-Mortem Studies in Glioblastoma Patients Treated with Thermotherapy Using Magnetic Nanoparticles. *Biomaterials* **2009**, *30*, 52–57.
21. Limbach, L. K.; Li, Y. C.; Grass, R. N.; Brunner, T. J.; Hintermann, M. A.; Muller, M.; Gunther, D.; Stark, W. J. Oxide Nanoparticle Uptake in Human Lung Fibroblasts: Effects of Particle Size, Agglomeration, and Diffusion at Low Concentrations. *Environ. Sci. Technol.* **2005**, *39*, 9370–9376.
22. Wick, P.; Manser, P.; Limbach, L. K.; Dettlaff-Weglikowska, U.; Krumeich, F.; Roth, S.; Stark, W. J.; Bruinink, A. The Degree and Kind of Agglomeration Affect Carbon Nanotube Cytotoxicity. *Toxicol. Lett.* **2007**, *168*, 121–131.
23. Murdock, R. C.; Braydich-Stolle, L.; Schrand, A. M.; Schlager, J. J.; Hussain, S. M. Characterization of Nanomaterial Dispersion in Solution Prior to *In Vitro* Exposure Using Dynamic Light Scattering Technique. *Toxicol. Sci.* **2008**, *101*, 239–253.
24. Andres, R. P.; Bein, T.; Dorogi, M.; Feng, S.; Henderson, J. I.; Kubiak, C. P.; Mahoney, W.; Osifchin, R. G.; Reifenberger, R. "Coulomb Staircase" at Room Temperature in a Self-Assembled Molecular Nanostructure. *Science* **1996**, *272*, 1323–1325.
25. Brust, M.; Bethell, D.; Kiely, C. J.; Schiffrin, D. J. Self-Assembled Gold Nanoparticle Thin Films with Nonmetallic Optical and Electronic Properties. *Langmuir* **1998**, *14*, 5425–5429.
26. Klajn, R.; Bishop, K. J.; Grzybowski, B. A. Light-Controlled Self-Assembly of Reversible and Irreversible Nanoparticle Suprastructures. *Proc. Natl. Acad. Sci. U.S.A.* **2007**, *104*, 10305–10309.
27. Nykypanchuk, D.; Maye, M. M.; van der Lelie, D.; Gang, O. DNA-Guided Crystallization of Colloidal Nanoparticles. *Nature* **2008**, *451*, 549–552.
28. Park, S. Y.; Lytton-Jean, A. K.; Lee, B.; Weigand, S.; Schatz, G. C.; Mirkin, C. A. DNA-Programmable Nanoparticle Crystallization. *Nature* **2008**, *451*, 553–556.
29. Sebba, D. S.; Mock, J. J.; Smith, D. R.; Labean, T. H.; Lazarides, A. A. Reconfigurable Core–Satellite Nanoassemblies as Molecularly-Driven Plasmonic Switches. *Nano Lett.* **2008**, *8*, 1803–1808.
30. Xu, X.; Rosi, N. L.; Wang, Y.; Huo, F.; Mirkin, C. A. Asymmetric Functionalization of Gold Nanoparticles with Oligonucleotides. *J. Am. Chem. Soc.* **2006**, *128*, 9286–9287.
31. Yao, H.; Yi, C. Q.; Tzang, C. H.; Zhu, J. J.; Yang, M. S. DNA-Directed Self-Assembly of Gold Nanoparticles into Binary and Ternary Nanostructures. *Nanotechnology* **2007**, *18*, 1–7.
32. Maye, M. M.; Nykypanchuk, D.; Cuisinier, M.; van der Lelie, D.; Gang, O. Stepwise Surface Encoding for High-Throughput Assembly of Nanoclusters. *Nat. Mater.* **2009**, *8*, 388–391.
33. Lee, S. K.; Maye, M. M.; Zhang, Y. B.; Gang, O.; van der Lelie, D. Controllable G5p-Protein-Directed Aggregation of ssDNA-Gold Nanoparticles. *Langmuir* **2009**, *25*, 657–660.
34. Hussain, I.; Wang, Z.; Cooper, A. I.; Brust, M. Formation of Spherical Nanostructures by the Controlled Aggregation of Gold Colloids. *Langmuir* **2006**, *22*, 2938–2941.
35. Daniels, T. R.; Delgado, T.; Helguera, G.; Penichet, M. L. The Transferrin Receptor Part II: Targeted Delivery of Therapeutic Agents into Cancer Cells. *Clin. Immunol.* **2006**, *121*, 159–176.
36. Zheng, Y.; Yu, B.; Weecharangsan, W.; Piao, L.; Darby, M.; Mao, Y.; Koynova, R.; Yang, X.; Li, H.; Xu, S. Transferrin-Conjugated Lipid-Coated Plga Nanoparticles for Targeted Delivery of Aromatase Inhibitor 7α-Aptadd to Breast Cancer Cells. *Int. J. Pharm.* **2010**, *390*, 234–241.
37. Krishna, A. D.; Mandraju, R. K.; Kishore, G.; Kondapi, A. K. An Efficient Targeted Drug Delivery through Apotransferrin Loaded Nanoparticles. *PLoS One* **2009**, *4*, e7240.
38. Shah, N.; Chaudhari, K.; Dantuluri, P.; Murthy, R. S.; Das, S. Paclitaxel-Loaded Plga Nanoparticles Surface Modified with Transferrin and Pluronic((R))P85, an *In Vitro* Cell Line and *In Vivo* Biodistribution Studies on Rat Model. *J. Drug Target* **2009**, *17*, 533–542.
39. Zhang, X.; Koh, C. G.; Yu, B.; Liu, S.; Piao, L.; Marcucci, G.; Lee, R. J.; Lee, L. J. Transferrin Receptor Targeted Lipopolyplexes for Delivery of Antisense Oligonucleotide G3139 in a Murine K562 Xenograft Model. *Pharm. Res.* **2009**, *26*, 1516–1524.
40. Choi, C. H.; Alabi, C. A.; Webster, P.; Davis, M. E. Mechanism of Active Targeting in Solid Tumors with Transferrin-Containing Gold Nanoparticles. *Proc. Natl. Acad. Sci. U.S.A.* **2010**, *107*, 1235–1240.
41. Frens, G. Controlled Nucleation for Regulation of Particle-Size in Monodisperse Gold Suspensions. *Nat. Phys. Sci.* **1973**, *241*, 20–22.
42. Lin, M. Y.; Lindsay, H. M.; Weitz, D. A.; Ball, R. C.; Klein, R.; Meakin, P. Universality in Colloid Aggregation. *Nature* **1989**, *339*, 360–362.
43. Orts-Gil, G.; Natte, K.; Drescher, D.; Bresch, H.; Mantion, A.; Kneipp, J.; Osterle, W. Characterisation of Silica Nanoparticles Prior to *In Vitro* Studies: From Primary Particles to Agglomerates. *J. Nanopart. Res.* **2011**, *13*, 1593–1604.
44. Hermanson, G. T. *Bioconjugate Techniques*; Academic Press: Amsterdam, 2008.
45. von Smoluchowski, M. Outline of the Coagulation Kinetics of Colloidal Solutions. *Kolloid Z.* **1917**, *21*, 98–104.
46. von Smoluchowski, M. Experiments on a Mathematical Theory of Kinetic Coagulation of Coloid Solutions. *Z. Phys. Chem.* **1917**, *92*, 129–168.

47. Witten, T. A.; Sander, L. M. Diffusion-Limited Aggregation, a Kinetic Critical Phenomenon. *Phys. Rev. Lett.* **1981**, *47*, 1400.
48. Ghosh, S. K.; Pal, T. Interparticle Coupling Effect on the Surface Plasmon Resonance of Gold Nanoparticles: From Theory to Applications. *Chem. Rev.* **2007**, *107*, 4797–4862.
49. Basu, S.; Ghosh, S. K.; Kundu, S.; Panigrahi, S.; Praharaj, S.; Pande, S.; Jana, S.; Pal, T. Biomolecule Induced Nanoparticle Aggregation: Effect of Particle Size on Interparticle Coupling. *J. Colloid Interface Sci.* **2007**, *313*, 724–734.
50. Hussain, I.; Brust, M.; Barauskas, J.; Cooper, A. I. Controlled Step Growth of Molecularly Linked Gold Nanoparticles: From Metallic Monomers to Dimers to Polymeric Nanoparticle Chains. *Langmuir* **2009**, *25*, 1934–1939.
51. Ge, Y. Q.; Zhang, Y.; Xia, J. G.; Ma, M.; He, S. Y.; Nie, F.; Gu, N. Effect of Surface Charge and Agglomerate Degree of Magnetic Iron Oxide Nanoparticles on Kb Cellular Uptake *In Vitro*. *Colloids Surf. B* **2009**, *73*, 294–301.
52. Fischer, H.; Fournier-Bidoz, S.; Chan, W.; Pang, K. Quantitative Detection of Engineered Nanoparticles in Tissues and Organs: An Investigation of Efficacy and Linear Dynamic Ranges Using Icp-Aes. *NanoBioTechnol.* **2007**, *3*, 46–54.
53. Gao, H.; Shi, W.; Freund, L. B. Mechanics of Receptor-Mediated Endocytosis. *Proc. Natl. Acad. Sci. U.S.A.* **2005**, *102*, 9469–9474.
54. Zhang, S. L.; Li, J.; Lykotrafitis, G.; Bao, G.; Suresh, S. Size-Dependent Endocytosis of Nanoparticles. *Adv. Mater.* **2009**, *21*, 419–424.
55. Yuan, H. Y.; Huang, C. J.; Zhang, S. L. Virus-Inspired Design Principles of Nanoparticle-Based Bioagents. *PLoS One* **2010**, *5*, e13495.
56. Yuan, H. Y.; Li, J.; Bao, G.; Zhang, S. L. Variable Nanoparticle-Cell Adhesion Strength Regulates Cellular Uptake. *Phys. Rev. Lett.* **2010**, *105*, 1381011–1381014.
57. Wittmaack, K. Excessive Delivery of Nanostructured Matter to Submersed Cells Caused by Rapid Gravitational Settling. *ACS Nano* **2011**, *5*, 3766–3778.
58. Stayton, I.; Winiarz, J.; Shannon, K.; Ma, Y. Study of Uptake and Loss of Silica Nanoparticles in Living Human Lung Epithelial Cells at Single Cell Level. *Anal. Bioanal. Chem.* **2009**, *394*, 1595–1608.
59. Skebo, J. E.; Grabinski, C. M.; Schrand, A. M.; Schlager, J. J.; Hussain, S. M. Assessment of Metal Nanoparticle Agglomeration, Uptake, and Interaction Using High-Illuminating System. *Int. J. Toxicol.* **2007**, *26*, 135–141.
60. Brandenberger, C.; Muhlfeld, C.; Ali, Z.; Lenz, A. G.; Schmid, O.; Parak, W. J.; Gehr, P.; Rothen-Rutishauser, B. Quantitative Evaluation of Cellular Uptake and Trafficking of Plain and Polyethylene Glycol-Coated Gold Nanoparticles. *Small* **2010**, *6*, 1669–1678.
61. Unfried, K.; Albrecht, C.; Klotz, L.-O.; Von Mikecz, A.; Grether-Beck, S.; Schins, R. P. F. Cellular Responses to Nanoparticles: Target Structures and Mechanisms. *Nanotoxicology* **2007**, *1*, 52–71.
62. Gosens, I.; Post, J. A.; de la Fonteyne, L. J. J.; Jansen, E. H. J. M.; Geus, J. W.; Cassee, F. R.; de Jong, W. H. Impact of Agglomeration State of Nano- and Submicron Sized Gold Particles on Pulmonary Inflammation. *Part. Fibre Toxicol.* **2010**, *7*, 1–11.
63. Kuhnel, D.; Busch, W.; Meissner, T.; Springer, A.; Potthoff, A.; Richter, V.; Gelinsky, M.; Scholz, S.; Schirmer, K. Agglomeration of Tungsten Carbide Nanoparticles in Exposure Medium Does Not Prevent Uptake and Toxicity toward a Rainbow Trout Gill Cell Line. *Aquat. Toxicol.* **2009**, *93*, 91–99.
64. Fischer, H. C.; Chan, W. C. W. Nanotoxicity: The Growing Need for *In Vivo* Study. *Curr. Opin. Biotechnol.* **2007**, *18*, 565–571.
65. Oberdorster, G.; Oberdorster, E.; Oberdorster, J. Nanotoxicology: An Emerging Discipline Evolving from Studies of Ultrafine Particles. *Environ. Health Perspect.* **2005**, *113*, 823–839.
66. Perrault, S. D.; Chan, W. C. W. Synthesis and Surface Modification of Highly Monodispersed, Spherical Gold Nanoparticles of 50−200 nm. *J. Am. Chem. Soc.* **2009**, *131*, 17042–17043.